Key Points:

- Near-bottom magnetic data reveal a short-wavelength low superimposed on the broader axial high along the fast-spreading East Pacific Rise near 9°50′N
- Magnetic anomaly data provide insight into crustal accretionary processes and temporal variations in geomagnetic field intensity
- Vector magnetic anomaly data allows for the analysis of magnetic anomalies independent of uncertainties associated with reduction to the pole

Significance of Short-Wavelength Magnetic Anomaly Low Along the East Pacific Rise Axis, 9°50′N

Natalia Berrios-Rivera[1] , Jeffrey S. Gee[1], Ross Parnell-Turner[1] , Sarah Maher[1] , Jyun-Nai Wu[1] , Daniel Fornari[2], Maurice Tivey[2] , Milena Marjanović[3] , Thibaut Barreyre[4] , and Jill McDermott[5]

[1]Scripps Institution of Oceanography, University of California, San Diego, La Jolla, CA, USA, [2]Department of Geology and Geophysics, Woods Hole Oceanographic Institution, Woods Hole, MA, USA, [3]Institut de Physique du Globe de Paris, CNRS UMR7154, Université Paris Cité, Paris, France, [4]Department of Earth Science, University of Bergen, Bergen, Norway, [5]Department of Earth and Environmental Science, Lehigh University, Bethlehem, PA, USA

Abstract Magnetic anomaly variations near mid-ocean ridge spreading centers are sensitive to a variety of crustal accretionary processes as well as geomagnetic field variations when the crust forms. We collected near-bottom vector magnetic anomaly data during a series of 21 autonomous underwater vehicle *Sentry* dives near 9°50′N on the East Pacific Rise (EPR) covering ∼26 km along-axis. These data document the 2–3 km wide axial anomaly high that is commonly observed at fast-spreading ridges but also reveal the presence of a superimposed ∼800 m full wavelength anomaly low. The anomaly low is continuous for ≥13 km along axis and may extend over the entire survey region. A more detailed survey of hydrothermal vents near 9°50.3′N reveals ∼100 m diameter magnetic lows, which are misaligned relative to active vents and therefore cannot explain the continuous axial low. The axial magnetization low persists in magnetic inversions with variable extrusive source thickness, indicating that to the extent to which layer 2A constitutes the sole magnetic source, variations in its thickness alone cannot account for the axial low. Lava accumulation models illustrate that high geomagnetic intensity over the past ∼2.5 kyr, and decreasing intensity over the past ∼900 years, are both consistent with the broad axial anomaly high and the superimposed shorter wavelength low. The continuity of this axial low, and similar features elsewhere on the EPR suggests, that either crustal accretionary processes responsible for this anomaly are common among fast-spread ridges, or that the observed magnetization low may partially reflect global geomagnetic intensity fluctuations.

Plain Language Summary Near-bottom magnetic anomaly data provide valuable information on crustal accretion processes at mid-ocean ridges. Using autonomous underwater vehicle data, we analyze near-bottom magnetic anomalies at the EPR 9°50′N to study crustal accretion at mid-ocean ridges. We find a continuous axial anomaly low superimposed on the typical broad axial magnetic high, located along the spreading axis covering an along-axis distance of more than 10 km. This axial anomaly low has been observed at other fast-spreading mid-ocean ridges, but the cause of the anomaly low is not well understood. Using magnetic inversion results and numerical models, we consider three possible causes for the axial anomaly low: variations in the thickness of the pillow lavas that are typically modeled as being the primary contributor to the magnetic signal, variations in Earth's geomagnetic field intensity, and hydrothermal vents chemically altering the magnetic minerals in the seafloor basalts. While the global occurrence of the axial anomaly low at other ridges makes it likely that geomagnetic field variations contribute to the low, it is likely that the observed axial magnetic low is caused by a combination of these three factors.

1. Introduction

As new oceanic crust forms at mid-ocean ridges, it acquires magnetization that preserves a record of geomagnetic field variations. The largest fluctuations in marine magnetic anomalies, typically measured at the sea surface, are due to geomagnetic field reversals leading to lineated anomalies that provide the template of the reversal sequence over the past 160 million years (Cande & Kent, 1995; Gradstein et al., 2020). Shorter wavelength anomaly variations may arise from a variety of causes. Within some longer polarity intervals, sea surface anomaly profiles reveal shorter wavelength variations that appear to be consistent regionally or globally, and therefore have been interpreted as likely reflecting geomagnetic intensity variations (e.g., Cande & Kent, 1992; Gee et al., 1996; Li et al., 2021). Magnetic anomaly amplitudes may also be modulated by a variety of crustal accretionary processes. For example, sea surface anomaly fluctuations both along and across-axis at fast-spread ridges

Writing – original draft: Natalia Berrios-Rivera, Jeffrey S. Gee, Ross Parnell-Turner
Writing – review & editing: Natalia Berrios-Rivera, Jeffrey S. Gee, Ross Parnell-Turner, Sarah Maher, Jyun-Nai Wu, Daniel Fornari, Maurice Tivey, Milena Marjanović, Thibaut Barreyre, Jill McDermott

have been interpreted as reflecting variations in the thickness and/or geochemistry of the magnetic source layer (Carbotte & MacDonald, 1992; Lee et al., 1996; Williams et al., 2008).

The ridge axis is often associated with a distinct short-wavelength (∼10 km) sea surface anomaly high, termed the central anomaly magnetization high (CAMH), originally interpreted as the locus of young, highly magnetized lavas (Klitgord, 1976). This feature is evident as a correspondingly shorter wavelength (∼3 km) anomaly high in near-bottom profiles at intermediate- and fast-spread ridges, where it may provide valuable insights into crustal accretionary processes. For example, along-axis variations in the amplitude of this axial magnetization high at 9°N on the East Pacific Rise (EPR) have been attributed to fluctuations in the thickness of the extrusive layer, and the pattern of lava accumulation off axis may likewise be reflected in the near-bottom anomaly pattern (Schouten et al., 1999; Williams et al., 2008).

An even shorter wavelength axial magnetization low, superimposed on the few-kilometer wide axial CAMH, has been documented in near-bottom profiles from several segments of fast-spreading EPR (Perram & Macdonald, 1990; Shah et al., 2003; Szitkar et al., 2016) and from the intermediate-spreading Endeavor segment (Tivey & Johnson, 1987). A variety of potential mechanisms have been proposed to explain this axial low, including localized alteration, elevated temperatures or the presence of shallow, weakly magnetic dikes beneath the axis (Tivey & Johnson, 1987). Variations in geomagnetic intensity have also been suggested as a possible source. For example, geomagnetic intensity recorded by surface samples from the southern EPR appears to mimic both the axial high and superimposed magnetic anomaly low (Gee et al., 2000), and near the EPR 9°50′N higher paleofield values were documented from samples 1–2 km off axis than in the axial summit region (Bowles et al., 2006).

Here we present a study of the near-axis magnetic anomaly pattern at the fast-spreading EPR near 9°50′N, using near-bottom vector magnetic data collected over ∼26 km along the ridge axis (from 9°44′ to 9°57′N) by autonomous underwater vehicle (AUV) *Sentry*. A near-bottom magnetic survey near 9°50′N, conducted by AUV *ABE* in 2001, revealed a double-peaked axial high with an intervening anomaly low centered on the axial summit trough (AST) (Schouten et al., 2003; Williams et al., 2008). The new data presented here reveal that this axial anomaly low, superimposed on the broader CAMH, is remarkably consistent for at least 13 km along axis and possibly over the entire survey area. The continuity of this axial low and the presence of similar features elsewhere on the EPR suggests that if accretionary processes are responsible for this feature, then these must be relatively common among fast-spread ridges. Alternatively, the observed magnetization variations might reflect geomagnetic intensity fluctuations that are expected to be present globally.

2. The 9°50′N Study Area

The EPR 9°N segment extends for ∼200 km between the Clipperton and Siqueiros transforms, and is one of the most well-studied portions of the global mid-ocean ridge system (e.g., Fornari et al., 2012, and references therein). Spreading occurs at a full rate of 108–109 mm/yr (Carbotte & MacDonald, 1992) and the spreading center itself is a broad axial high, topped by a linear, ∼40–100 m wide AST which hosts eruptive fissures and active hydrothermal vents (Figure 1; Haymon et al., 1993; Macdonald & Fox, 1988). The volcanic and hydrothermal systems are thought to be underlain by a <100 m-thick axial magma lens (AML) that extends beneath most of the ridge segment at an average depth of ∼1.6 km (e.g., Aghaei et al., 2014; Detrick et al., 1987; Herron et al., 1978; Marjanović et al., 2014, 2018; Mutter et al., 1988; Xu et al., 2014), with additional melt lenses observed up to 10 km off-axis (e.g., Han et al., 2014). Seafloor eruptions are documented to have occurred in 1991–1992 and most recently in 2005–2006 (e.g., Haymon et al., 1993; Tolstoy et al., 2006), when lava flows extended ∼3 km away from the AST, covering an area of ∼21 km^2 with an average flow thickness of ∼1.5 m (Figure 1; Soule et al., 2007; Wu et al., 2022).

The thickness of extrusive pillow lavas and sheet flows, thought to be approximated by seismic layer 2A, plays a key role in determining the shape and amplitude of magnetic anomalies near the ridge axis (Gee & Kent, 1994; Schouten et al., 1999; Tivey et al., 1993) and is unusually well-constrained at the 9°50′N segment. Seismic reflection and refraction experiments show that between 9°39.9′ and 9°56.2′N, extrusive layer 2A is 130 ± 10 m thick within 1 km of the axis (Marjanović et al., 2018; Sohn et al., 2004). At distances 1–2 km from the ridge axis, seismic reflection imaging shows that layer 2A thickness likely increases to ∼500 m (Harding et al., 1993; Marjanović et al., 2018).

Hydrothermal vents are widespread and ubiquitous along the 9°50′N segment, with high-temperature black-smoker style vents and lower temperature diffuse vents both within the AST (e.g., Haymon et al., 1991; Von Damm &
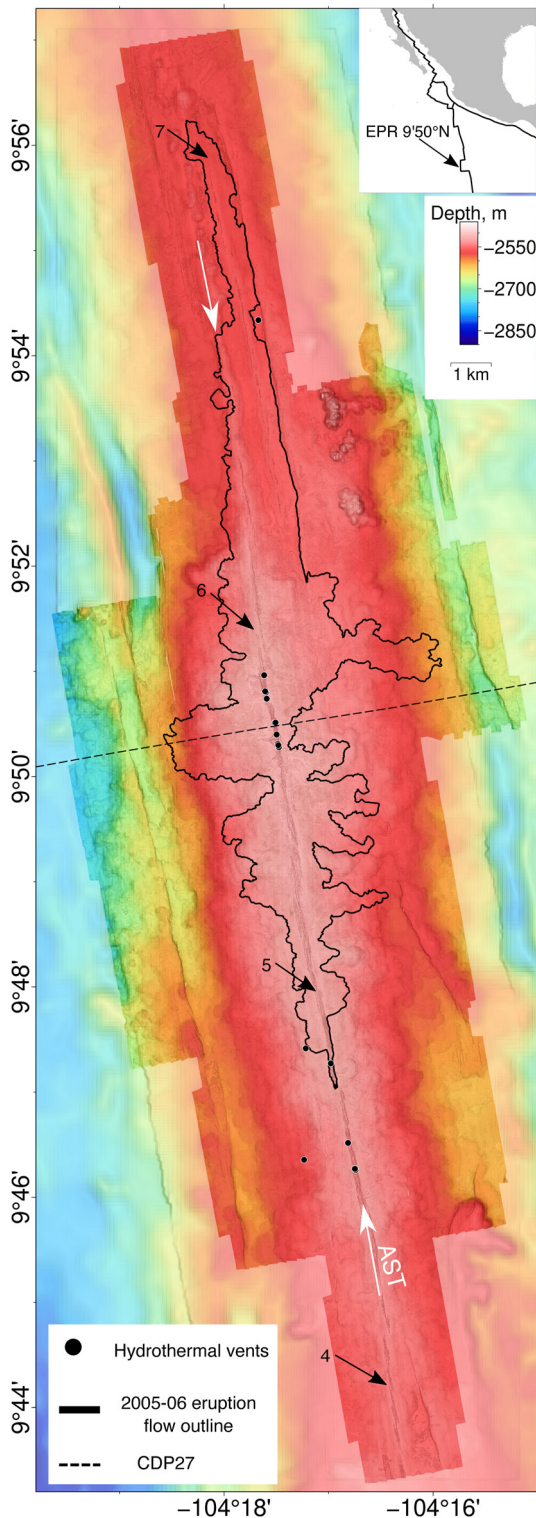
Figure 1. Bathymetry of 9°50′N study area; darker shades show near-bottom bathymetric and magnetic and data coverage; lighter shades are 30 m-resolution shipboard data (White et al., 2006). Black line is 2005–2006 eruption extent (Wu et al., 2022); black circles are hydrothermal vent locations; white box shows the location of Figure 4; white arrows show axial summit trough; numbered black arrows are axial magma lens discontinuities that define fourth-order spreading segments (Marjanović et al., 2018).

Lilley, 2004) and off-axis (McDermott et al., 2022). Fluid temperatures are 350 ± 30°C and exhibit chemical variations both between vents and over timescales of months to years (Von Damm et al., 1995), while the vent chimney sulfide structures themselves are likely to persist for at least tens of years (Haymon et al., 1991). These high-temperature fluids can alter or replace titanomagnetite grains (e.g., Rona, 1978), which reduces the magnetic remanence of rocks in layer 2A and leads to magnetization lows associated with hydrothermal vent systems, as seen on the Juan de Fuca Ridge (Tivey & Johnson, 2002). Sea surface magnetic surveys reveal the local magnetization high along the entire EPR axis in this region minor interruptions corresponding to the boundaries between fourth-order ridge segments (e.g., Carbotte & MacDonald, 1992; Lee et al., 1996). Near-bottom towed magnetic data collected between 9°25′N and 9°57′N indicate a well-defined crustal magnetization high centered on the ridge axis (CAMH), a north-south gradient that could be explained by kilometer-scale variations in magnetic source layer thickness along-axis (Williams et al., 2008). A near-bottom magnetic survey conducted over a 1 km × 2 km patch of the AST using AUV *ABE* in 2001–2002 showed a magnetization low associated with the AST, and subtle magnetization lows around hydrothermal vents (Bio9 and P vents; Fornari et al., 2004). However, the limited areal extent of this AUV *ABE* survey meant that the spatial extent and the origin of the axial low within the CAMH remained uncertain. To overcome this uncertainty, we collected near-bottom magnetic anomaly data from a broader area near 9°50′N.

3. Data Acquisition and Processing

Near-bottom vector magnetic field data were acquired using an Applied Physics Systems Model 1520 triaxial fluxgate magnetometer mounted near the top of AUV *Sentry* during 20 dives over the course of three cruises in 2018, 2019, and 2021 (see Supporting Information S1 and Data Availability Statement). Here we focus on the data from 19 spatially contiguous dives during which the vehicle traveled at an average altitude of ∼70 m at a speed of ∼1 m/s, with a survey line spacing of ∼180 m (Table S1 in Supporting Information S1). In addition, we examine data from one dive (524) that re-surveyed the same general hydrothermal vent area as the AUV *ABE* surveys in 2001 (Williams et al., 2008) ∼20 m above the seafloor and with an average line spacing of ∼5 m.

Vector component and total field anomalies were calculated following a processing scheme similar to that described by Maher et al. (2020). Initial data processing included a temperature-dependent scalar calibration for each sensor (Olsen et al., 2003), data filtering and compensation for different mounting orientations and platform motion to calculate north, east and down components of the anomalous field (see Supporting Information S1). Near the start of each dive when the survey altitude (∼70 m above bottom) was reached, the vehicle executed a set of calibration spins, during which the vehicle rotated through 360° while remaining at a constant depth and location where the magnetic field should be essentially constant. We separately fit the heading-dependent sinusoidal variations in each vector component during these spins to compensate for any permanent or induced signal generated by the vehicle platform (see Supporting Information S1). The peak-to-trough amplitude of these heading-dependent corrections ranged from about 200 to 500 nT. After subtraction of the regional magnetic field component values based on the International Geomagnetic Reference Field (IGRF12) model

(Thébault et al., 2015), the resulting along track anomalies were smoothed with a 20-s Gaussian filter and re-sampled at a uniform 10-s interval.

Although bathymetric variations in the survey area are relatively minor (<50 m), for the purposes of comparison with previous surveys and for inversion to determine the magnetization distribution, the along track component and total field anomalies were resampled at 10 m spacing and then upward continued (see Supporting Information S1) to a constant depth of 2,400 m using the methodology of Guspi (1987). To assess the internal consistency of the survey data, we minimized crossover errors using the method of Prince and Forsyth (1984). After correction, the initial root mean square (rms) misfit of total field anomalies at crossing points (77.6 nT) was reduced to 29.7 nT, with comparable reductions in the component anomaly misfits (see Supporting Information S1). A separate crossover analysis treating each dive as a single segment was used to adjust the small (~10%) portion of the data unconstrained by crossing segments and these data, appropriately down-weighted, were combined with the more robust segment-adjusted data to yield final 10 m grids using adjustable tension continuous curvature splines via the surface algorithm in the Generic Mapping Tools (GMT, version 6; Wessel et al., 2019).

The 20-m elevation (and hence higher resolution) data acquired during dive 524 required some modifications in our data processing scheme. Although the spin calibration adequately compensates for most heading-dependent anomaly variations, the closely spaced turns in this dense survey resulted in artifacts during upward continuation. To minimize these effects, magnetic anomaly data collected during turns were removed prior to upward continuation to a constant depth of 2,480 m, preserving the higher resolution of these data. Here, we found that setting the reference level to the minimum depth, with a long wavelength filter cutoff of 20 km and a short wavelength filter cutoff of 400 m, best preserved the anomaly signal where little or no upward continuation was needed. Crossover analysis for the 281 trackline segments longer than 50 m reduced the rms misfit for the total field anomaly from 105.3 to 21.5 nT, with comparable rms misfits for the component anomalies (see Supporting Information S1). These data were combined with nearby tracks from the broader survey to generate the final anomaly grids with 2 m node spacing using the surface algorithm in GMT.

4. Results

We find that the typical broad (~2–3 km wide) central magnetic anomaly high over the ridge axis is accompanied by a near continuous, shorter wavelength anomaly low that extends at least 13 km along-axis. Using the measured vector components of the near-bottom anomaly field and numerical models, we explore whether this low could be explained either by hydrothermal alteration, changes in source thickness, or fluctuations in geomagnetic intensity.

4.1. Near-Ridge Magnetic Anomaly Pattern

The near-bottom survey data presented here corroborate many aspects of the anomaly pattern reported by Williams et al. (2008), but also enable some important new observations (Figure 2). The most pronounced difference between the near-bottom anomaly data presented here and earlier surveys is the presence of a continuous, short wavelength (~300–400 m wide at half height; full wavelength ~800 m) anomaly low superimposed on the broader (~2–3 km wide) axial anomaly high. This marked axial low is evident in the total field anomaly data, particularly in the central portion of the survey, but is most prominent in the vertical component and reduced to the pole (RTP) anomalies (Figures 2c and 2d), where its position closely corresponds to the location of the AST. The amplitude of this anomaly low varies slightly along axis but it appears to be continuous for at least 13 km along axis (9°47′–9°54′N). To better characterize this axial low, we extracted profiles spaced 100 m apart from the RTP grid, aligned these using the AST location (Wu et al., 2022) and calculated a stacked (mean) profile for each kilometer along axis (Figure 3). The axial low is most symmetric in the central portion of the survey (coinciding with fourth-order discontinuities (Carbotte et al., 2013) 5–6 in the AML; Figures 1 and 3c), where it has a full wavelength of about 800 m and a peak-to-trough amplitude of about 750 nT. This axial anomaly low is also present in segments both to the north and south (segments 4–5 and segments 6–7) and is slightly asymmetric, with higher anomaly values west of the AST. While the RTP stacked anomaly has significantly higher amplitude, stacked profiles of the total field and vertical component also exhibit a consistent overall width of 2–3 km for the CAMH and the shorter wavelength (~800 m) superimposed axial low, which appears well centered on the AST.

Based primarily on ridge-parallel survey lines spaced 500–800 m apart, the earlier study of Williams et al. (2008) suggested that the total field axial high was displaced about 1 km west of the AST from 9°43′ to 9°57′N. In
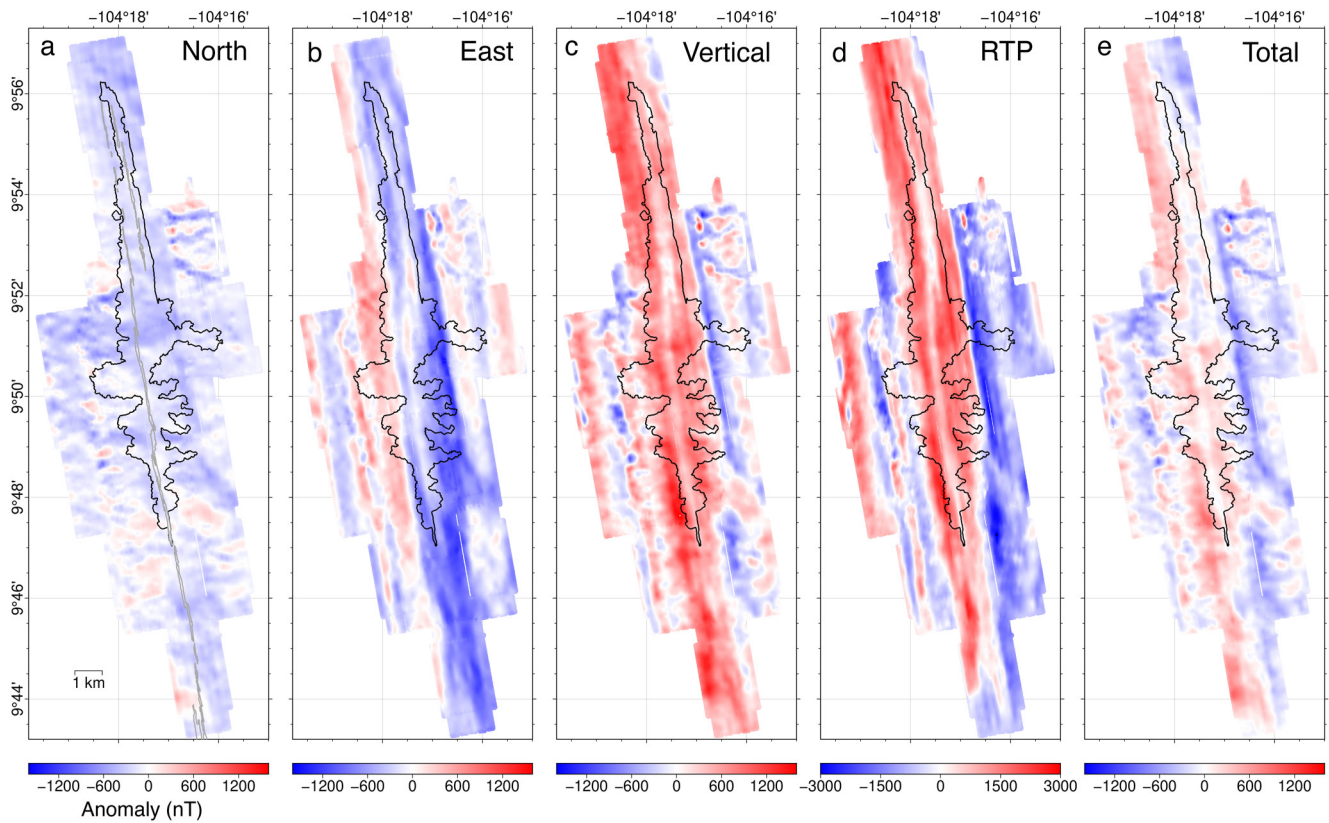
Figure 2. Vector components and total field magnetic anomalies illustrating the anomaly high and shorter wavelength axial low near 9°50′N on the East Pacific Rise. Data were measured ~70 m above the seafloor using autonomous underwater vehicle *Sentry* and upward continued to 2,400 m below sea level. The boundary of the 2005–2006 flow is shown for reference. (a) North component, (b) East component, (c) Vertical component, (d) Reduced to the pole (RTP) anomaly, and (e) Total field anomaly. The shorter wavelength axial low is most evident in the vertical component and RTP anomalies.

contrast, the higher resolution data presented here indicate that this axial high is approximately centered over the AST in the central portion of the survey (9°47′–9°51′N), though there is agreement that both north and south of this central region the total field axial high is located west of the AST. The reduced to the pole (RTP) anomaly, which centers anomalies over their sources (Blakely, 1995), results in an axial high that is more symmetric about the AST throughout the surveyed region.

The measured vector components of the anomalous field provide complementary information on the distribution of magnetic sources. In particular, the measured vertical anomaly is most useful as anomalies are centered over their sources, but without any of the assumptions inherent in the RTP transformation. The vertical anomaly (Figure 2c) is similar to the RTP pattern (Figure 2d) in revealing an axial high that is approximately centered over the AST throughout the region. Some differences between the vertical and RTP anomalies are apparent; for example, the vertical anomaly low on the eastern ridge flank appears less continuous than the RTP anomaly. As expected for an approximately north-south oriented, two-dimensional source, the north component of the anomaly is minimal, though it does more clearly highlight some oblique features (e.g., the normal fault on the east flank near 9°48′N) and three-dimensional features such as the volcanic features east of the axis near 9°53′N.
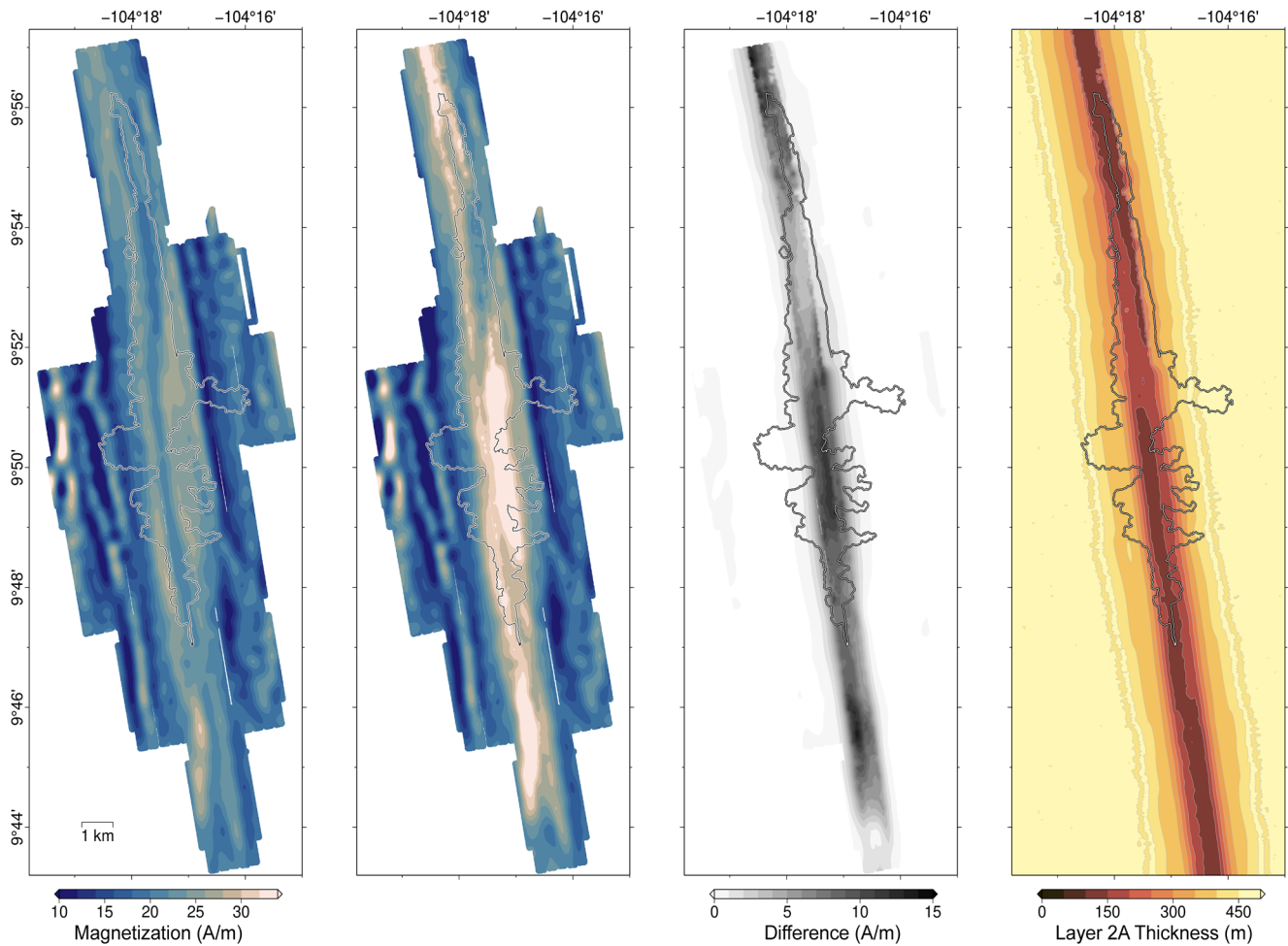
4.2. Magnetization Solutions

In order to better understand the origin of the axial anomaly low as well as the overall magnetization distribution, we calculated magnetization solutions using the method of Parker and Huestis (1974). We first calculated the magnetization distribution for a uniform thickness (500 m) source layer whose upper surface follows the bathymetric data acquired by AUV *Sentry* (padded with 30-m resolution data from R/V *Thompson*). The inversion used an ambient field direction at the site (6.6°/32.1°) and a remanence direction (0°/19.1°) consistent with the time-averaged dipole field direction. The magnetization solution was filtered using a cosine-tapered bandpass
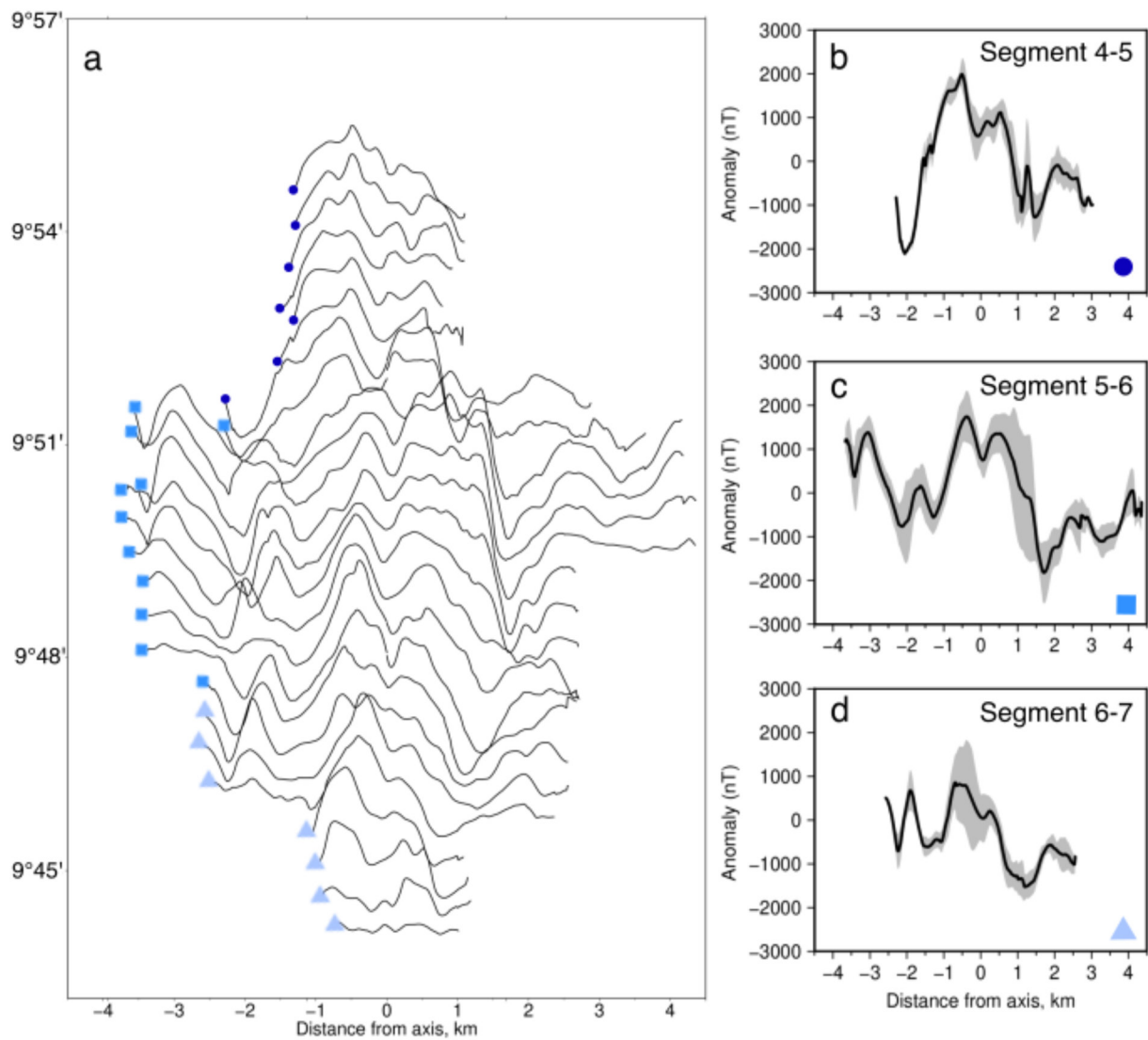
Figure 3. Stacked reduced to pole (RTP) anomalies illustrating the continuity of the short wavelength axial low at East Pacific Rise near 9°50′N. (a) Stacked anomalies shown in their approximate positions along axis. Distances are relative to the center of the axial summit trough (Wu et al., 2022). Colored symbols indicate profiles used for the averages shown in panels at right. (b–d) Stacked anomalies with 1 sigma uncertainties (gray band) for profiles within segments 6–7, 5–6 and 4–5, respectively (segments defined as fourth-order axial magma lens discontinuities from Marjanović et al. (2018), extents are approximately 9°52′ to 9°56′N, 9°48′ to 9°52′N and 9°44′ to 9°48′N, respectively).

with long and short wavelength cutoffs at 20 and 0.4 km, respectively. Twenty times the 1 A/m annihilator was added to the solution to generate uniformly positive magnetization. For the seismic Layer 2A thickness model, we use the results of a 3D along-axis seismic reflection survey from Marjanović et al., 2018 to model the thickness within ~350 m on either side of the ridge axis. These data indicate that the minimum near-axis Layer 2A thickness is ~95 m (Marjanović et al., 2018). Outside this swath, Layer 2A thickness increases as a function of distance from the ridge axis, and is constant along-axis. Because seismic layer 2A thickness ranges from 95 to 250 m over the ~1-km-wide axial zone and increases in thickness further off-axis (Marjanović et al., 2018), we also explored a variable-thickness solution (see Supporting Information S1) under the assumption that layer 2A approximates the extrusive layer as the dominant magnetic source.

Magnetic inversion results for the total field anomaly data using uniform and variable layer 2A thickness confirm the ~2–3 km wide CAMH along the AST, but also the shorter-wavelength superimposed axial magnetization low (Figure 4). For the uniform-thickness solution (Figure 4a), magnetizations range from 2.0 to 37.5 A/m and the narrow axial low is evident from at least 9°47′ to 9°54′N and arguably is present, though less continuous, throughout the survey region. Magnetizations for the variable-thickness solution range from 1.8 to 43.7 A/m. Here, the

Figure 4. Magnetization solutions illustrating possible effects of variable magnetic source layer thickness. (a and b) Total field crustal magnetization, calculated using uniform (500 m) and variable layer 2A thickness, respectively. (c) difference between total field crustal magnetization and total field crustal magnetization contrast (d) Layer 2A thickness, interpolated from reflection and seismic estimates (Harding et al., 1993; Marjanović et al., 2018). Layer 2A thickness (d) is used for the variable thickness model (b). Contour interval is 50 m. See Supporting Information S1 for details on the variable thickness model.

axial low persists but is less pronounced from 9°48′ to 9°51′N, where significantly higher magnetizations east of the AST are associated with a thinned source layer. The magnetization solution from the vertical anomaly (Figure S1 in Supporting Information S1) reveals an axial low very similar to that derived from the total field anomaly.

The detailed survey near 9°50.3′N provides an opportunity to examine any possible discrete magnetization lows associated with hydrothermal activity at the Tica, Bio9 and P vents (Figure 5). Fluids from seafloor hydrothermal systems alter the magnetization of seafloor basalts containing iron-rich magnetic minerals, resulting in discrete magnetization lows, or "burnholes" associated with active or inactive hydrothermal vents (Tivey & Johnson, 2002). Our finer scale total field anomaly data in this region acquired at ∼20 m above the seafloor during AUV *Sentry* dive 524 (Figure 5a) reveal discrete anomaly lows consistent with burnholes ∼100 m in diameter, though these lows do not appear to be centered on the active vents. Crustal magnetization was calculated from the inversion of total field magnetic anomaly data using a ∼135 m thick magnetization layer that corresponds to the average layer 2A thickness in the area (Marjanović et al., 2018). All three vents lie within modest magnetization lows, 2–4 A/m lower than the flanking magnetization highs, that are elongate parallel to the AST and may reflect a more continuous axial low.

5. Discussion

New data acquired on the EPR near 9°50′N document the presence of a short wavelength (∼800 m) axial magnetic anomaly low that is continuous for at least 13 km along axis and that appears to be centered above the AST.
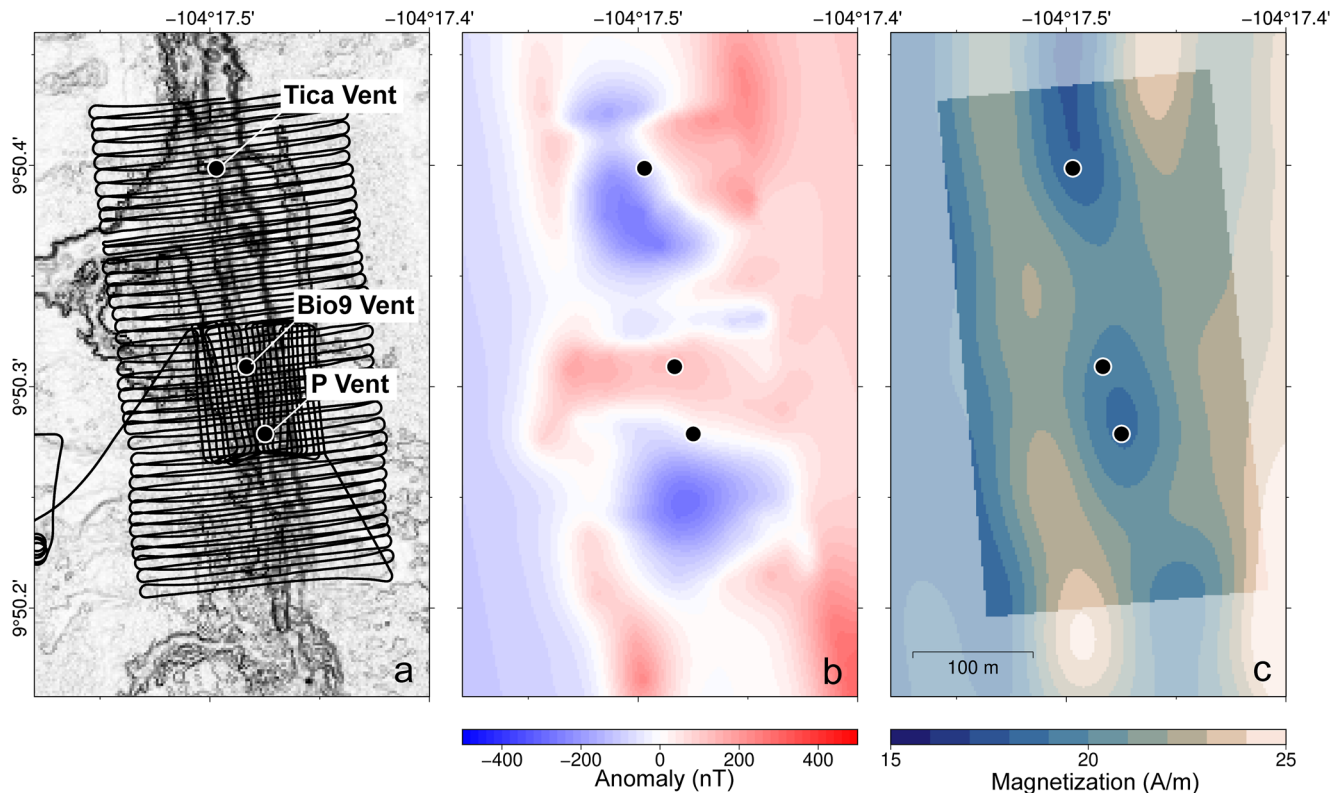
Figure 5. Near-bottom magnetic anomalies over axial summit trough and hydrothermal vents near 9°50.3′N. (a) Survey tracklines (black lines) and hydrothermal vent locations (black dots); survey lines spaced ∼10 m, and ∼25 m vehicle altitude enable detection of short-wavelength magnetic anomalies associated with hydrothermal vents. (b) Total field anomaly. (c) Total field crustal magnetization for an along-axis segment with hydrothermal vents, calculated with 135 m thick magnetic layer, corresponding to average layer 2A thickness in this region (Marjanović et al., 2018). Anomaly data were upward continued to 2,480 m, and filtered using a bandpass filter with 5 km and 80 m cutoffs. Twenty times a 1 A/m annihilator was added.

Similar short wavelength axial anomaly lows have been documented from near-bottom total field anomaly data elsewhere on the EPR. A detailed survey extending ∼3 km along axis near 17°28′S revealed a 200 m wide low roughly centered on the AST; when upward continued to an altitude more comparable to our survey, this anomaly low is about 300 m wide with an amplitude of a few hundred nT (Shah et al., 2003). A more extensive survey along the EPR from 15°36′ to 15°52′N documented a ∼600-m-wide axial low, which south of 15°44′N appears continuous along axis for about 17 km (Szitkar et al., 2016). These data were acquired at a similar altitude (70 m) as the survey presented here, and the 750 nT amplitude of the RTP anomaly low is comparable to that observed near 9°50′N (Figure 2d). A series of four near-bottom profiles on the more magma-starved EPR between 19°42′ and 19°49′S reveal a somewhat broader (500 m–2 km wide) anomaly low with amplitudes of several hundred to more than 1,000 nT that is roughly centered on the axis (Gee et al., 2000).

The presence of axial anomaly lows over multiple segments of the fast-spreading EPR is suggestive of a common cause; however, a number of different explanations have been advanced for this feature. This range of explanations is perhaps not surprising given the multiple factors that can modulate anomaly amplitudes, including those related to the source geometry (e.g., topography, pattern of lava accretion, thickness) and those influencing the magnetization (e.g., geochemistry, alteration, geomagnetic intensity). For the EPR near 9°50′N, several of these factors are unlikely to produce significant magnetization contrasts in the axial region. For example, although increasing FeO content is correlated with enhanced magnetization (Gee & Kent, 1997), glass compositions of near-axis lavas from 9°42′ to 9°56′N show relatively little variation (9.75 ± 0.70% FeO; PetDB Team, 2019) and thus are unlikely to be responsible for significant magnetization variations in the region. Similarly, the effects of time-dependent low-temperature alteration on the magnetization are likely not pervasive enough or of sufficient magnitude to generate large variations in this near-ridge environment (e.g., Gee & Kent, 2007) and the influence of bathymetric variations are explicitly accounted for in our magnetization inversions. We therefore focus our

discussion on the origin of the axial anomaly low and three factors that have well-documented effects on the anomaly amplitude: hydrothermal alteration, source thickness variations, and geomagnetic intensity.

5.1. Hydrothermal Alteration

Hydrothermal fluids at temperatures of 300–400°C can transform the titanomagnetite remanence carriers in seafloor basalts to nonmagnetic phases, in some cases reducing the magnetization by an order of magnitude or more (e.g., Oliva-Urcia et al., 2011; Rona, 1978; Wang et al., 2020) and resulting in discrete (∼100 m diameter) magnetization lows, or burnholes, associated with active or inactive hydrothermal upflow zones (Tivey & Johnson, 2002). The axial magnetic low in the 9°50′N study area is known to host active hydrothermal vents (Figure 1), but also extends over areas with no known active or inactive hydrothermal vents in the present day. While we do observe some relatively isolated magnetization lows near active vents (Figure 5), the discrete distribution of known active and inactive vents is inconsistent with a continuous axial low. Similarly, the lack of any known vents near 17°28′S on the EPR, and the continuous nature of the axial anomaly low there (as compared to the expected ∼100 m dimension of burnholes), led Shah et al. (2003) to conclude that hydrothermal activity could not explain the axial low.

While these conclusions seem reasonable given the focused upflow areas evident on the seafloor, the time-integrated effect of individual vents on the magnetic source layer likely depends on their lifespan and along-axis distribution. At fast-spread ridges, observations and modeling suggest that high temperature venting may persist continuously for more than a decade (Lowell & Germanovich, 1994; Von Damm & Lilley, 2004). U-series dating of sulfides from the fast-spreading EPR near 12°50′N yields ages of less than a decade in many cases, and maximum ages of ∼150–170 years (Lalou et al., 1985) and the age range of vent deposits appear to increase at slower spreading rates (Jamieson et al., 2013). The distribution of hydrothermal vents at 9°N seems closely tied to the AST, with nearly all high-temperature vents occurring within the AST or near its bounding faults (Haymon et al., 1991). Given the relatively short lifespan of vents and their close association with the AST, the coalesced magnetic signature of multiple vents could generate a continuous axial anomaly low.

We constructed a simple model to evaluate the potential impact of multiple generations of hydrothermal vents on the axial magnetic source (Figure 6). Each localized hydrothermal vent is expected to generate a cylindrical region of reduced magnetization with near complete remanence removal (0.1 of initial value) within ±10 m of the vent. Magnetization reduction progressively diminishes to a maximum diameter of 100 m, consistent with the presumed dimension inferred from burnholes on the Endeavor segment (Tivey & Johnson, 2002). Based on the present-day distribution of high-temperature vents near 9°50′N, we model two clusters of vents at each time step, one with six vents drawn from a Gaussian distribution along axis (sigma = 1,000 m), and the other with four vents drawn from a slightly broader distribution (sigma = 2,500 m). At each time step, the center of each of these clusters was drawn from a uniform distribution along axis, with the position of individual vents along axis established from the Gaussian distribution described above. Finally, Gaussian deviates (sigma = 30 m) were used to establish the proximity of vents to the axis and the total field anomaly was then calculated 100 m above the source. An example of the evolution of the axial anomaly low during multiple iterations is shown in Figure 6c. After six time steps, a near-continuous axial anomaly low that broadly resembles that seen on the EPR (wavelength ∼500 m, amplitude of several hundred nT) can develop. Additional iterations result in a more continuous and increasingly higher amplitude axial low that differs from the observed anomaly pattern.

Repeated eruption cycles, causing repeated rearrangement of individual hydrothermal vents and their respective discrete magnetization lows, could plausibly generate a coalesced, quasi-continuous axial anomaly low. The 50 m-wide AST in our study area corresponds to about 545 years of spreading, while estimates of the recurrence interval of eruptions at fast-spread ridges are typically on the order of a few decades (e.g., Bowles et al., 2006; Haymon, 1996; Perfit & Chadwick, 1998; Wu et al., 2022). If each time step in our model represents a few decades, then clusters of hydrothermal vents might be repositioned to several tens of times before the crust is effectively rafted outside the AST.

If this mechanism of coalesced hydrothermal alteration were responsible for the axial low, it follows that all lava flows erupted or ponded in the AST at fast-spread ridges (where hydrothermal activity is concentrated) at fast-spread ridges could contain a record of this phenomenon. With such a mechanism influencing vent positioning, near-bottom magnetic anomaly data might provide a valuable source of information on the distribution and duration of hydrothermal vent systems at the fast-spread EPR.
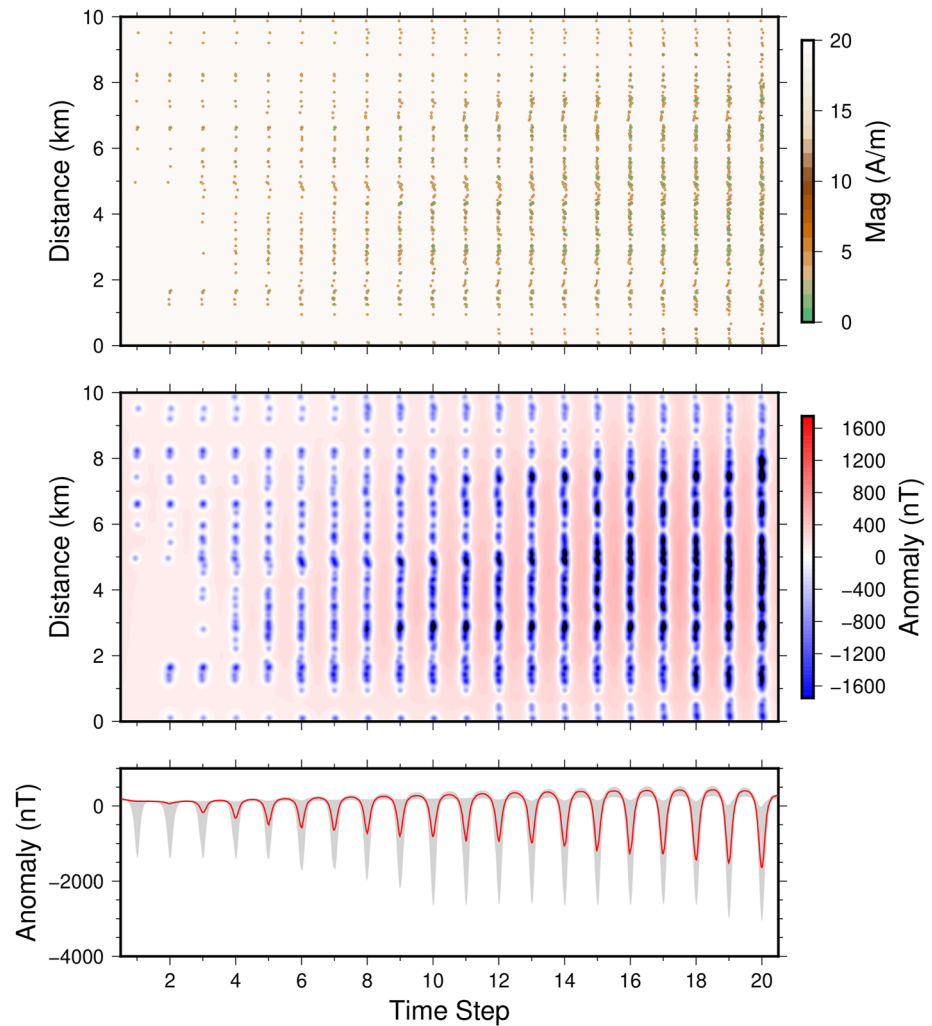
Figure 6. Model illustrating the possible role of high-temperature hydrothermal vents in generating the short-wavelength axial anomaly low. Each new timestep (possibly representing a few decades of elapsed time) introduces 10 new vents located as described in the text. For convenience, the magnetic anomaly was calculated from a series of adjacent time steps, with axis location centered on each time step and representing local magnetization distribution within ±500 m of the axis. (a) Map view of evolution of axial magnetization distribution for 20 time steps. Axis is located in the center of each time step. (b) Map view of total field anomaly calculated 100 m above the seafloor assuming vertical ambient field and remanence direction. (c) Stacked median anomaly profile (red) and its uncertainty (gray).

5.2. Source Thickness Variations

Lava flows likely represent the largest magnetic source contributing to lineated marine magnetic anomalies, particularly near the axis of fast-spread ridges where an AML is present; therefore, variations in the thickness of the extrusive layer should be reflected in the anomaly pattern. To illustrate the influence of variations in extrusive layer thickness, it is useful to compare averaged profiles through our magnetization solutions for uniform (500 m) and a variable thickness source (Figure 7). As with the anomaly stacks in Figure 3, we have calculated mean profiles for each kilometer along the axis as a function of distance from the center of the AST (Wu et al., 2022). For the uniform thickness model, the axial magnetization low is remarkably continuous, well constrained, though not perfectly, centered on the AST (Figure 7a). Variations in seismic Layer 2A thickness are well constrained only within about 500 m of the axis; therefore, the primary effect is to enhance the magnetization in this axial region. Notably, from 9°43′N to 9°51′N, the thickness of Layer 2A varies little in the immediate vicinity of the AST and the axial magnetization low remains evident throughout this region (Figure 7c). Although the amplitude of the flanking magnetization highs is more variable than in the uniform thickness model, the persistence of the axial low indicates that it cannot solely be a function of reduced source layer thickness.
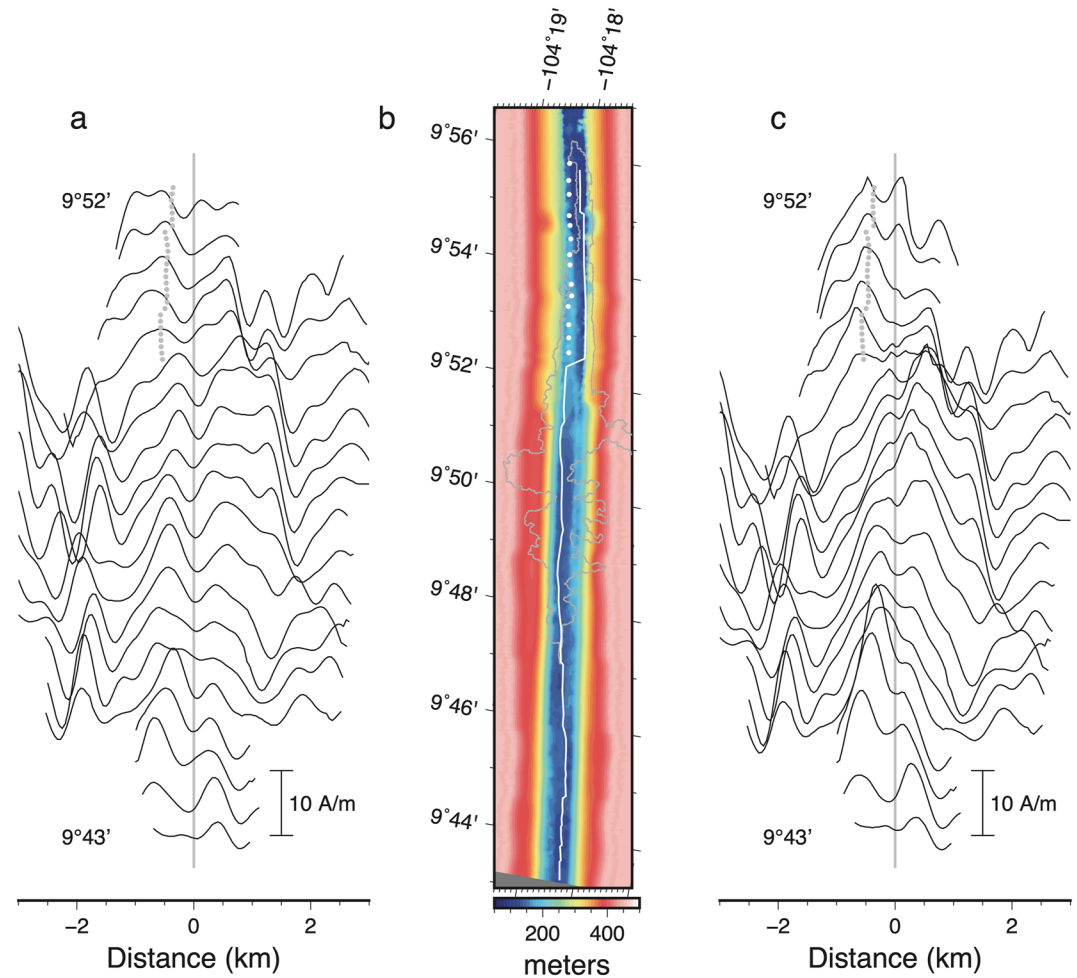
Figure 7. Magnetization profiles relative to the center of axial summit trough (AST). (a) Stacked (mean) magnetization profiles for each kilometer along the axis for (a) uniform (500 m) thick magnetization source aligned at the AST (vertical line). Gray dots indicate alternative western AST position shown in the middle panel. (b) Magnetization source layer thickness interpolated from reflection and seismic estimates of Layer 2A (Harding et al., 1993; Marjanović et al., 2018) (see Figure 4). The boundary of the 2005/2006 flow is shown for reference. White line indicates the center of AST; dots indicate alternative western AST location. (c) Stacked (mean) magnetization profiles for a variable thickness source defined by seismic Layer 2A thickness.

Moreover, our variable thickness model assumes that lavas are the only magnetic source and therefore almost certainly overestimates the influence of seismic layer 2A variations in modulating near-ridge anomaly amplitudes. While the magnetization of lava flows typically exceeds that of deeper sources, there is growing evidence that the magnetization of dikes at fast-spread ridges may also be significant. For example, dikes sampled at DSDP Hole 504B as well as at Hess Deep have magnetization (~2 A/m) that are roughly 40% of that of extrusives from well-sampled localities (Gee & Kent, 2007, and references therein). More recent sampling of dikes from fast-spread crust exposed at Pito Deep have an average magnetization of 4.5 A/m ($n = 23$; Horst et al., 2011). Estimates of the magnetization at Pito Deep from near-bottom magnetic anomaly surveys also suggest that the sheeted dikes likely have magnetizations that are roughly half that of the overlying lava flows (Maher et al., 2020). Elevated temperatures within the sheeted dike complex would be expected to reduce their magnetization, particularly near the base of the dikes where temperatures (400–700°C; Gillis, 2008) could approach or exceed the Curie temperature of the dominant magnetic phase in the dikes (580°C; Gee & Kent, 2007). Nonetheless, seismic estimates suggest the dike layer near 9°50′N is approximately a kilometer thick (Marjanović et al., 2018) and therefore at least the uppermost portion of the dike layer is likely to contribute to the overlying anomaly pattern. Given that the axial magnetic low persists even under the assumption of no contribution from sources below seismic layer 2A, it appears that other factors must also play a role in producing this short-wavelength low.
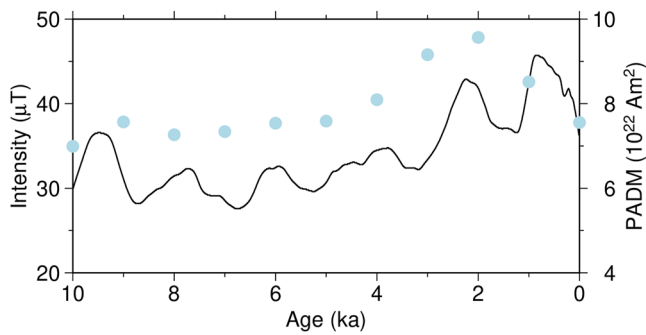
Figure 8. Geomagnetic field intensity variation for the past 10 kyr. Black line is the CALS10k.2 intensity model evaluated at 9°50′N in the study area (Constable et al., 2016); blue dots are paleomagnetic axial dipole moment (PADM) from the PADM2m global model (Ziegler et al., 2011).

5.3. Geomagnetic Intensity Variations

To the extent that the oceanic crust has a thermal remanence acquired during initial cooling, its magnetization will be linearly proportional to the ambient field intensity during cooling. Global models of the Holocene geomagnetic field (e.g., Constable et al., 2016) indicate that intensity near 9°50′N has been steadily decreasing from a peak value of ~46 μT about 900 years ago to its present value of 36 μT (Figure 8; Constable et al., 2016). In addition, these models indicate that intensity was higher than the present value (by as much as 25%) over the past ~2.5 kyr while the preceding ~6 kyr were characterized by values as low as 75% of the present value. These intensity variations should be reflected in the magnetization of the youngest near-ridge lavas and dikes, which could contribute both to the broader CAMH and possibly to the shorter wavelength axial magnetization low that we have documented.

The anomaly pattern expected as a result of these geomagnetic intensity variations is not easy to predict, however, as this will also be a function of crustal accretionary processes such as the dimensions and recurrence interval of lava flows, how narrow the zone of dike emplacement and eruptions are at the ridge, and how far lava flows might extend from the axis. The zone over which dikes are emplaced near the ridge is likely to be narrow. For example, Hooft et al. (1996) suggested that a narrow Gaussian distribution (sigma ~10 m) for dike emplacement was required to reconcile estimates of the lava/dike transition zone thickness in ophiolites with those inferred from seismic observations (Hussenoeder et al., 2002; Smith & Cann, 1999). Magnetization variations within the dikes are therefore likely to closely parallel any time-dependent variations of geomagnetic intensity, that is, isochron boundaries and magnetization contrasts should be nearly vertical and distance from the ridge should closely approximate the age inferred from constant spreading. The pattern of lava accumulation near the ridge has a much more significant impact on the resulting magnetic anomaly, and variations in anomaly amplitude have been used to infer the near-axis distribution and thickness of the extrusive layer (Bowles et al., 2006; Hooft et al., 1996; Schouten et al., 1999). The redistribution of lava flows off axis, their spatial extent and thickness as well as the overall eruptive frequency will play a key role in how the time-varying geomagnetic signal is expressed in the anomaly pattern.

To illustrate how these factors might modulate the near-ridge anomaly, we simulated the near-bottom magnetic anomaly using a three dimension stochastic model of lava accumulation (Gee et al., 2016) that builds on earlier two-dimensional models of Hooft et al. (1996). Individual flows mapped on the EPR provide estimates of flow volumes (<0.01–0.22 km³), aspect ratios (up to ~15:1) and eruption frequency (several eruptions per 100–1,000 years) and document the importance of off-axis transport in lava channels (e.g., Bergmanis et al., 2007; Fundis et al., 2010; Soule et al., 2005). Modeled flow volumes are proportional to the time since the last eruption, such that volumes follow a gamma distribution, and these models use a median flow volume of 0.07 km³ (corresponding to a median waiting time between flows of about 10–37 years) and an average aspect ratio of 5:1 that are compatible with observations from the EPR. For reasons outlined above, our model assumes that the magnetization of dikes is 40% of that of the extrusives (see Supporting Information S1 for additional details on the modeling).

Although the specific parameters chosen are subject to significant uncertainty, the resulting models (Figure 9) nonetheless provide an indication of how near-bottom anomaly patterns are sensitive to the pattern of lava accumulation, off-axis thickening of the extrusive layer, as well as the geomagnetic intensity variations at the time of eruption. For example, when larger flows erupt or pond nearer the ridge (within 500 m), the most recent high field intensity results in a pronounced axial high and strongly lineated anomalies. A broader distribution (1,500 m) of large flows yields a more variable anomaly pattern and off-axis thickening of extrusives more compatible with seismic observations. Both of these models assume an exponential distribution of flow volumes (gamma shape factor, $k = 1$) with frequent small volume flows. If very short recurrence intervals are subdued ($k = 3$), the resulting axial anomaly is reduced and the overall anomaly pattern is more complex. Although well-documented lava flows near 9°50′N on the EPR in 1991 and 2005/2006 suggest a recurrence interval of the order of a decade, it is currently not possible to discern the underlying distribution of eruptive times and flow volumes from which these eruptions were drawn.
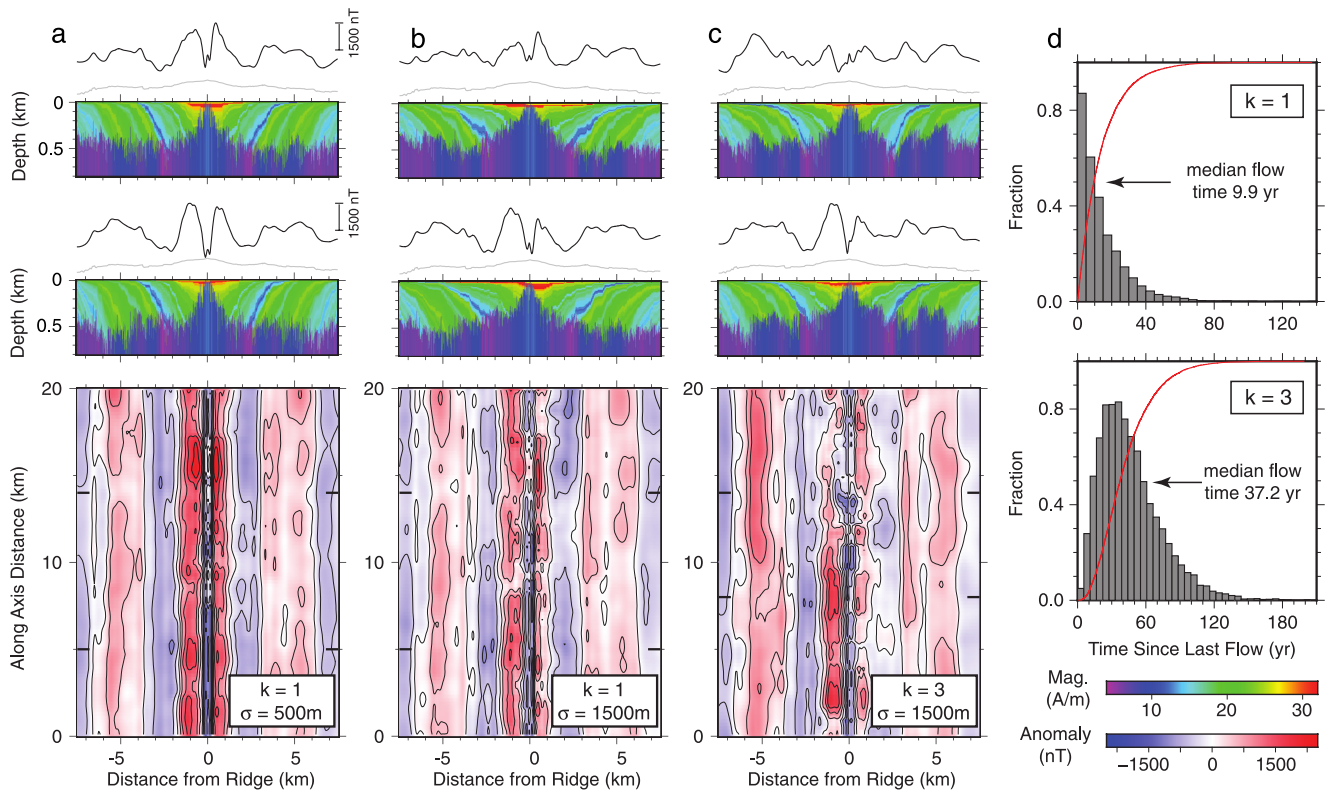
Figure 9. Results from 3D stochastic model illustrating how crustal accretion may influence the near-bottom anomaly pattern. The anomaly is calculated 500 m above the source and assuming a remanence and ambient field direction of 0°/90°. Panels (a–c) show anomaly and magnetization and anomaly profiles for two representative profiles (locations indicated by black bars on anomaly plot). Sigma value indicates the mean off-axis transport distance. Magnetizations are proportional to dipole moment variations of PADM2m (Figure S5 in Supporting Information S1) (Ziegler et al., 2011) with zero age at the ridge. Dikes have magnetizations that are 40% of lava values. (d) Distributions of time between successive flows used in the models. Flow geometries vary from frequent low aspect ratio pillow mounds to larger flows with an average aspect ratio of 5:1 and average thickness of 5 m (see Figures S3 and S4 in Supporting Information S1 for additional details of the model).

Regardless of the details of the lava flow distribution, these simplified models illustrate how we might expect geomagnetic intensity variations to be reflected in the upper crust and in the associated anomaly pattern. The higher field intensities of the late Holocene (yellow-red colors in cross sections in Figure 9) should be represented by a few-kilometer wide axial zone of enhanced magnetizations similar to the overall wavelength (2–3 km) of the CAMH in near-bottom anomaly profiles from the EPR. Note that these high magnetization lavas are distributed over an order of magnitude broader area than expected from the distance calculated from constant spreading (the 2–3 kyr intensity high would be restricted to within ~100 m of the axis based on 55 mm/yr half spreading rate). As suggested previously (Schouten et al., 1999), the near-bottom anomaly pattern should also be sensitive to the presence and distance from the axis of any lava depocenters. Geomagnetic intensity of surface samples from near 9°50′N on the EPR document higher paleofield values 1–2 km off axis than in the axial summit region (Bowles et al., 2006). The models in Figure 9 also exhibit a shorter wavelength axial low superimposed on the broader CAMH. Although surface flows reflecting the recent decline in field intensity would be dispersed over a broader area, the record of this lower intensity in the uppermost dikes should be closely linked with distance from the axis. Because the magnetizations of both lava flows and dikes is linearly related to field intensity, we expect this signal to be present and to be reflected, to some degree, in the associated anomaly pattern. While our modeling does not allow a definitive estimate of their relative contributions, we suggest that this axial low represents the combined effects of a thinner extrusive source layer at the axis, but also some contribution from the recent decrease in geomagnetic intensity recorded in the thicker but lower magnetization dike layer.

6. Conclusions

This study using near-bottom magnetic data collected by AUV provides insight into the possible causes of the short-wavelength axial anomaly low superimposed on the broader CAMH at fast-spread ridges. The axial anomaly

low near 9°50′N is generally well centered above the AST, is essentially continuous for at least 13 km along axis, and possibly extends for the ∼26 km axial length of our study area. Compared to previous surveys that note an axial anomaly low, the data collected at EPR 9°50′N presented here show perhaps the most continuous example of this short-wavelength axial anomaly low. This continuous axial anomaly low is visible in the total field and vector components of the magnetic anomaly data as well as in the magnetization solutions of inverse models. Directly measuring vector components of magnetic anomaly data reduces the uncertainties in the interpretation of both the total field and RTP anomalies. The continuity of the axial anomaly low indicates that it is not caused by alteration of magnetic minerals from the present-day distribution of hydrothermal vents. Magnetic anomalies caused by hydrothermal alteration are expected to produce isolated, closed-contour anomaly lows, which can be resolved in near-bottom magnetic surveys, and would not produce a linear, continuous magnetic anomaly on short timescales. It is possible, however, that the integrated signal of hydrothermal alteration from many generations of vents with varying locations along axis could produce an axial low similar to that observed.

Although we cannot constrain a single source for the axial anomaly low, temporal variation in geomagnetic field intensity and layer 2A thickness are both sources that are likely contributors to the axial anomaly low. Variable thickness magnetization solutions, using seismically determined layer 2A variations, still show evidence of an axial low, but also indicate that layer 2A thickness variations cannot be the sole cause of this axial magnetization low. Higher geomagnetic intensity over the past 2.5 kyr should be reflected in the magnetization of the youngest near-ridge lavas and dikes, which should contribute both to the broader CAMH and possibly to the shorter wavelength axial magnetization low that we have documented. Future near-bottom magnetic surveys, at other fast-spreading mid-ocean ridges, direct sampling of the extrusive lava flows and dikes, and additional modeling may indicate the relative degree to which each parameter contributes as a source of the axial low. These results highlight the value of near-bottom magnetic surveys as a means to assess near-ridge crustal accretionary processes as well as a potential archive of geomagnetic field variations.

Data Availability Statement

Near-bottom magnetic anomaly data collected by AUV *Sentry* are available at the Marine Geoscience Data System at https://doi.org/10.26022/IEDA/331244 (Parnell-Turner et al., 2023). Figures were made using GMT version 6 (Wessel et al., 2019).

References

Aghaei, O., Nedimovic, M. R., Carton, H., Carbotte, S. M., Canales, J. P., & Mutter, J. C. (2014). Crustal thickness and Moho character of the fast-spreading East Pacific Rise from 9°42′N to 9°57′N from poststack-migrated 3-D MCS data. *Geochemistry, Geophysics, Geosystems*, *15*(3), 1–24. https://doi.org/10.1002/2013GC005069

Bergmanis, E. C., Sinton, J., & Rubin, K. H. (2007). Recent eruptive history and magma reservoir dynamics on the southern East Pacific Rise at 17°30′S. *Geochemistry, Geophysics, Geosystems*, *8*(12). https://doi.org/10.1029/2007GC001742

Blakely, R. J. (1995). *Potential theory in gravity and magnetic applications*. Cambridge University Press.

Bowles, J., Gee, J. S., Kent, D. V., Perfit, M. R., Soule, S. A., & Fornari, D. J. (2006). Paleointensity applications to timing and extent of eruptive activity, 9°–10°N East Pacific Rise. *Geochemistry, Geophysics, Geosystems*, *7*(6), 1–32. https://doi.org/10.1029/2005GC001141

Cande, S. C., & Kent, D. V. (1992). Ultrahigh resolution marine magnetic anomaly profiles: A record of continuous paleointensity variations? *Journal of Geophysical Research*, *97*(B11), 15075–15083. https://doi.org/10.1029/92JB01090

Cande, S. C., & Kent, D. V. (1995). Revised calibration of the geomagnetic polarity timescale for the Late Cretaceous and Cenozoic. *Journal of Geophysical Research*, *100*(B4), 6093–6095. https://doi.org/10.1029/94jb03098

Carbotte, S. M., & MacDonald, K. C. (1992). East Pacific Rise 8°–10°30′N: Evolution of ridge segments and discontinuities from SeaMARC II and three-dimensional magnetic studies. *Journal of Geophysical Research*, *97*(B5), 6959–6982. https://doi.org/10.1029/91JB03065

Carbotte, S. M., Marjanović, M., Carton, H., Mutter, J. C., Canales, J. P., Nedimovi, M. R., et al. (2013). Fine-scale segmentation of the crustal magma reservoir beneath the East Pacific Rise. *Nature Geoscience*, *6*(10), 866–870. https://doi.org/10.1038/ngeo1933

Constable, C., Korte, M., & Panovska, S. (2016). Persistent high paleosecular variation activity in southern hemisphere for at least 10,000 years. *Earth and Planetary Science Letters*, *453*, 78–86. https://doi.org/10.1016/j.epsl.2016.08.015

Detrick, R. S., Buhl, P., Vera, E., Mutter, J., Orcutt, J., Madsen, J., & Brocher, T. (1987). Multi-channel seismic imaging of a crustal magma chamber along the East Pacific Rise. *Nature*, *326*(6108), 35–41. https://doi.org/10.1038/326035a0

Fornari, D. J., Tivey, M. A., Schouten, H., Perfit, M., Yoerge, D., Bradley, A., et al. (2004). Submarine lava flow emplacement at the East Pacific Rise 9°50′N: Implications for uppermost ocean crust stratigraphy and hydrothermal fluid circulation. In C. R. German & L. M. Parson (Eds.), *Mid-ocean ridges: Hydrothermal interactions between the lithosphere and oceans*, *Geophysical Monograph Series* (Vol. 148, pp. 187–217). American Geophysical Union. https://doi.org/10.1029/148GM08

Fornari, D. J., Von Damm, K. L., Bryce, J., Cowen, J., Ferrini, V. L., Fundis, A. T., et al. (2012). The East Pacific Rise between 9°N and 10°N: Twenty-five years of integrated, multidisciplinary oceanic spreading center studies. *Oceanography*, *25*(1), 18–43. https://doi.org/10.5670/oceanog.2012.02

Fundis, A. T., Soule, S. A., Fornari, D. J., & Perfit, M. (2010). Paving the seafloor: Volcanic emplacement processes during the 2005–2006 eruptions at the fast spreading East Pacific Rise, 9°50′N. *Geochemistry, Geophysics, Geosystems*, *11*(8), Q08024. https://doi.org/10.1029/2010GC003058

Gee, J., & Kent, D. V. (1994). Variations in layer 2A thickness and the origin of the central anomaly magnetic high. *Geophysical Research Letters*, *21*(4), 297–300. https://doi.org/10.1029/93GL03422

Gee, J., & Kent, D. V. (1997). Magnetization of axial lavas from the southern East Pacific Rise (14°–23°S): Geochemical controls on magnetic properties. *Journal of Geophysical Research*, *102*(11), 24873–24886. https://doi.org/10.1029/97jb02544

Gee, J., Schneider, D. A., & Kent, D. V. (1996). Marine magnetic anomalies as recorders of geomagnetic intensity variations. *Earth and Planetary Science Letters*, *144*(3–4), 327–335. https://doi.org/10.1016/s0012-821x(96)00184-7

Gee, J. S., Cande, S. C., Hildebrand, J. A., Donnelly, K., & Parker, R. L. (2000). Geomagnetic intensity variations over the past 780 kyr obtained from near-seafloor magnetic anomalies. *Nature*, *408*(6814), 827–832. https://doi.org/10.1038/35048513

Gee, J. S., Cande, S. C., & Kent, D. V. (2016). Lava accumulation patterns at fast-spread ridges and the fidelity of marine magnetic anomalies. In *Abstract GP31D-01 presented at 2016 AGU Fall Meeting, San Francisco, California, December 12–16*.

Gee, J. S., & Kent, D. V. (2007). Source of oceanic magnetic anomalies and the geomagnetic polarity timescale. *Treatise on Geophysics*, *5*, 455–507. https://doi.org/10.1016/B978-044452748-6.00097-3

Gillis, K. M. (2008). The roof of an axial magma chamber: A hornfelsic heat exchanger. *Geology*, *36*(4), 299–302. https://doi.org/10.1130/G24590A.1

Gradstein, F. M., Ogg, J. G., Schmitz, M. D., & Ogg, G. M. (Eds.). (2020). *Geologic Time Scale 2020*. Elsevier. https://doi.org/10.1016/c2020-1-02369-3

Guspi, F. (1987). Frequency-domain reduction of potential field measurements to a horizontal plane. *Geoexploration*, *24*(2), 87–98. https://doi.org/10.1016/0016-7142(87)90083-4

Han, S., Carbotte, S. M., Carton, H., Mutter, J. C., Aghaei, O., Nedimović, M. R., & Canales, J. P. (2014). Architecture of on- and off-axis magma bodies at EPR 9°37–40′N and implications for oceanic crustal accretion. *Earth and Planetary Science Letters*, *390*, 31–44. https://doi.org/10.1016/j.epsl.2013.12.040

Harding, A. J., Kent, G. M., & Orcutt, J. A. A. (1993). A multichannel seismic investigation of upper crustal structure at 9°N on the East Pacific Rise: Implications for crustal accretion. *Journal of Geophysical Research*, *98*(B8), 13913–13944. https://doi.org/10.1029/93jb00886

Haymon, R. M. (1996). The response of ridge-crest hydrothermal systems to segmented, episodic magma supply. *Geological Society Special Publication*, *118*(118), 157–168. https://doi.org/10.1144/GSL.SP.1996.118.01.09

Haymon, R. M., Fornari, D. J., Edwards, M. H., Carbotte, S. M., Wright, D. J., & MacDonald, K. C. (1991). Hydrothermal vent distribution along the East Pacific Rise crest (9°09′–54′N) and its relationship to magmatic and tectonic processes on fast-spreading mid-ocean ridges. *Earth and Planetary Science Letters*, *104*(2–4), 513–534. https://doi.org/10.1016/0012-821X(91)90226-8

Haymon, R. M., Fornari, D. J., Von, K. L. D., Lilley, M. D., Perfit, M., Edmond, J. M., et al. (1993). Volcanic eruption of the mid-ocean ridge along the East Pacific Rise crest at 9°45–52′N: Direct submersible observations of seafloor phenomena associated with an eruption event in April, 1991. *Earth and Planetary Science Letters*, *119*(1–2), 85–101. https://doi.org/10.1016/0012-821x(93)90008-w

Herron, T. J., Ludwig, W. J., Stoffa, P. L., Kan, T. K., & Buhl, P. (1978). Structure of the East Pacific Rise crest from multichannel seismic reflection data. *Journal of Geophysical Research*, *83*(B2), 798. https://doi.org/10.1029/jb083ib02p00798

Hooft, E. E. E., Schouten, H., & Detrick, R. S. (1996). Constraining crustal emplacement processes from the variation in seismic layer 2A thickness at the East Pacific Rise. *Earth and Planetary Science Letters*, *142*(3–4), 289–309. https://doi.org/10.1016/0012-821x(96)00101-x

Horst, A. J., Varga, R. J., Gee, J. S., & Karson, J. A. (2011). Paleomagnetic constraints on deformation of superfast-spread oceanic crust exposed at Pito Deep Rift. *Journal of Geophysical Research*, *116*(12), 1–24. https://doi.org/10.1029/2011JB008268

Hussenoeder, S. A., Kent, G. M., & Detrick, R. S. (2002). Upper crustal seismic structure of the slow spreading, 35°N: Constraints on volcanic emplacement processes. *Journal of Geophysical Research*, *107*(B8), 2156. https://doi.org/10.1029/2001JB001691

Jamieson, J. W., Hannington, M. D., Clague, D. A., Kelley, D. S., Delaney, J. R., Holden, J. F., et al. (2013). Sulfide geochronology along the Endeavour Segment of the Juan de Fuca Ridge. *Geochemistry, Geophysics, Geosystems*, *14*(7), 2084–2099. https://doi.org/10.1002/ggge.20133

Klitgord, K. D. (1976). Sea-floor spreading: The central anomaly magnetization high. *Earth and Planetary Science Letters*, *29*(1), 201–209. https://doi.org/10.1016/0012-821x(76)90040-6

Lalou, C., Brichet, E., & Hekinian, R. (1985). Age dating of sulfide deposits from axial and off-axial structures on the East Pacific Rise near 12°50′N. *Earth and Planetary Science Letters*, *75*(1), 59–71. https://doi.org/10.1016/0012-821X(85)90050-0

Lee, S.-M., Solomon, S. C., & Tivey, M. A. (1996). Fine-scale crustal magnetization variations and segmentation of the East Pacific Rise, 9°10′–9°50′N. *Journal of Geophysical Research*, *101*(B10), 22033–22050. https://doi.org/10.1029/96jb02114

Li, Y., Liu, J., & Liu, Q. (2021). Geomagnetic field paleointensity spanning the past 11 Myr from marine magnetic anomalies in the Southern Hemisphere. *Geophysical Research Letters*, *48*(11), e2021GL093235. https://doi.org/10.1029/2021GL093235

Lowell, R. P., & Germanovich, L. N. (1994). On the temporal evolution of high-temperature hydrothermal systems at ocean ridge crests. *Journal of Geophysical Research*, *99*(B1), 565–575. https://doi.org/10.1029/93JB02568

Macdonald, K. C., & Fox, P. J. (1988). The axial summit graben and cross-sectional shape of the East Pacific Rise as indicators of axial magma chambers and recent volcanic eruptions. *Earth and Planetary Science Letters*, *88*(1–2), 119–131. https://doi.org/10.1016/0012-821x(88)90051-9

Maher, S. M., Gee, J. S., Doran, A. K., Cheadle, M. J., & John, B. E. (2020). Magnetic structure of fast-spread oceanic crust at Pito Deep. *Geochemistry, Geophysics, Geosystems*, *21*(2), 1–18. https://doi.org/10.1029/2019GC008671

Marjanović, M., Carbotte, S. M., Carton, H., Nedimović, M. R., Mutter, J. C., & Canales, J. P. (2014). A multi-sill magma plumbing system beneath the axis of the East Pacific Rise. *Nature Geoscience*, *7*(11), 825–829. https://doi.org/10.1038/ngeo2272

Marjanović, M., Carbotte, S. M., Carton, H. D., Nedimović, M. R., Canales, J. P., & Mutter, J. C. (2018). Crustal magmatic system beneath the East Pacific Rise: Implications for tectonomagmatic segmentation and crustal melt transport at fast-spreading ridges. *Geochemistry, Geophysics, Geosystems*, *19*(11), 4584–4611. https://doi.org/10.1029/2018GC007590

McDermott, J. M., Parnell-Turner, R. E., Barreyre, T., Herrera, S., Downing, C. C., Fornari, D. J., et al. (2022). Discovery of active off-axis hydrothermal vents at 9°54′N East Pacific Rise. *Proceedings of the National Academy of Sciences of the United States of America*, *119*(30), 1–8. https://doi.org/10.1073/pnas.2205602119

Mutter, J. C., Barth, G. A., Buhl, P., Detrick, R. S., Orcutt, J., & Harding, A. J. (1988). Magma distribution across ridge-axis discontinuities on the East Pacific Rise from multichannel seismic images. *Nature*, *336*(6195), 156–158. https://doi.org/10.1038/336156a0

Oliva-Urcia, B., Kontny, A., Vahle, C., & Schleicher, A. M. (2011). Modification of the magnetic mineralogy in basalts due to fluid-rock interactions in a high-temperature geothermal system (Krafla, Iceland). *Geophysical Journal International*, *186*(1), 155–174. https://doi.org/10.1111/j.1365-246X.2011.05029.x

Olsen, N., Primdahl, F., Tøffner-Clausen, L., Sabaka, T., Brauer, P., Merayo, J., et al. (2003). Calibration of the Ørsted vector magnetometer. *Earth Planets and Space*, *55*(1), 11–18. https://doi.org/10.1186/BF03352458

Parker, R. L., & Huestis, S. (1974). The inversion of magnetic anomalies in the presence of topography. *Journal of Geophysical Research*, *79*(11), 1587–1593. https://doi.org/10.1029/jb079i011p01587

Parnell-Turner, R., Gee, J., Berrios-Rivera, N., Fornari, D., McDermott, J., & Barreyre, T. (2023). *Near-bottom AUV Sentry raw magnetic data (MATLAB format) from 9°50′N, East Pacific Rise (2018, AT42-06)*. IEDA. https://doi.org/10.26022/IEDA/331244

Perfit, M. R., & Chadwick, W. W. (1998). Magmatism at mid-ocean ridges: Constraints from volcanological and geochemical investigations. In *Faulting and Magmatism at Mid-Ocean Ridges*, *Geophysical Monograph* (Vol. 106, pp. 59–115). American Geophysical Union. https://doi.org/10.1029/GM106p0059

Perram, L. J., & Macdonald, K. C. (1990). A one-million-year history of the 11°45′N East Pacific Rise discontinuity. *Journal of Geophysical Research*, *95*(B13), 21363. https://doi.org/10.1029/jb095ib13p21363

PetDB Team. (2019). *EarthChem Data-To-Go: Geochemical Data for the East Pacific Rise, version February 2019, Version 1.0*. Interdisciplinary Earth Data Alliance (IEDA). https://doi.org/10.1594/IEDA/111306

Prince, R. A., & Forsyth, D. W. (1984). A simple objective method for minimizing crossover errors in marine gravity data. *Geophysics*, *49*(7), 1070–1083. https://doi.org/10.1190/1.1441722

Rona, P. A. (1978). Magnetic signatures of hydrothermal alteration and volcanogenic mineral deposits in oceanic crust. *Journal of Volcanology and Geothermal Research*, *3*(1–2), 219–225. https://doi.org/10.1016/0377-0273(78)90010-0

Schouten, H., Tivey, M., Fornari, D., & Edwards, M. (2003). High-resolution, near-bottom observations of lava transport and accumulation on East Pacific Rise 9°–10°N. In *EGS-AGU-EUG Joint Assembly*.

Schouten, H., Tivey, M. A., Fornari, D. J., & Cochran, J. R. (1999). Central anomaly magnetization high: Constraints on the volcanic construction and architecture of seismic layer 2A at a fast-spreading mid-ocean ridge, the EPR at 9°30′–50′N. *Earth and Planetary Science Letters*, *169*(1–2), 37–50. https://doi.org/10.1016/s0012-821x(99)00063-1

Shah, A. K., Cormier, M., Ryan, W. B. F., Jin, W., Sinton, J., Bergmanis, E., et al. (2003). Episodic dike swarms inferred from near-bottom magnetic anomaly maps at the southern East Pacific Rise. *Journal of Geophysical Research*, *108*(B2), 2097. https://doi.org/10.1029/2001jb000564

Smith, D. K., & Cann, J. R. (1999). Constructing the upper crust of the mid-Atlantic Ridge: A reinterpretation based on the Puna Ridge, Kilauea Volcano. *Journal of Geophysical Research*, *104*(B11), 25379–25399. https://doi.org/10.1029/1999jb900177

Sohn, R. A., Webb, S. C., & Hildebrand, J. A. (2004). Fine-scale seismic structure of the shallow volcanic crust on the East Pacific Rise at 9°50′N. *Journal of Geophysical Research*, *109*, 1–17. https://doi.org/10.1029/2004JB003152

Soule, S. A., Fornari, D. J., Perfit, M., & Rubin, K. H. (2007). New insights into mid-ocean ridge volcanic processes from the 2005–2006 eruption of the East Pacific Rise, 9°46′N–9°56′N. *Geology*, *35*(12), 1079–1082. https://doi.org/10.1130/G23924A.1

Soule, S. A., Fornari, D. J., Perfit, M., Tivey, M. A., Ridley, W. I., & Schouten, H. (2005). Channelized lava flows at the East Pacific Rise crest 9°–10°N: The importance of off-axis lava transport in developing the architecture of young oceanic crust. *Geochemistry, Geophysics, Geosystems*, *6*(8), Q08005. https://doi.org/10.1029/2005GC000912

Szitkar, F., Dyment, J., Le Saout, M., Honsho, C., & Gente, P. (2016). Dyking at EPR 16°N hypermagmatic ridge segment: Insights from near-seafloor magnetics. *Earth and Planetary Science Letters*, *453*, 288–297. https://doi.org/10.1016/j.epsl.2016.08.020

Thébault, E., Finlay, C. C., Beggan, C. D., Alken, P., Aubert, J., Barrois, O., et al. (2015). International Geomagnetic Reference Field: The 12th generation. *Earth Planets and Space*, *67*(1). https://doi.org/10.1186/s40623-015-0228-9

Tivey, M. A., & Johnson, H. P. (1987). The central anomaly magnetic high: Implications for ocean crust construction and evolution. *Journal of Geophysical Research*, *92*(B12), 12612–12685. https://doi.org/10.1029/jb092ib12p12685

Tivey, M. A., & Johnson, H. P. (2002). Crustal magnetization reveals subsurface structure of Juan de Fuca Ridge hydrothermal vent fields. *Geology*, *30*(11), 979–982. https://doi.org/10.1130/0091-7613(2002)030<0979:CMRSSO>2.0.CO;2

Tivey, M. A., Rona, P. A., & Schouten, H. (1993). Reduced crustal magnetization beneath the active sulfide mound, TAG hydrothermal field, Mid-Atlantic Ridge at 26°N. *Earth Planetary Science Letters*, *115*(1–4), 101–115. https://doi.org/10.1016/0012-821x(93)90216-v

Tolstoy, M., Cowen, J. P., Baker, E. T., Fornari, D. J., Rubin, K. H., Shank, T. M., et al. (2006). A sea-floor spreading event captured by seismometers. *Science*, *314*(5807), 1920–1922. https://doi.org/10.1126/science.1133950

Von Damm, K. L., & Lilley, M. D. (2004). Diffuse flow hydrothermal fluids from 9°50′N East Pacific Rise: Origin, evolution and biogeochemical controls. *Geophysical Monograph Series*, *144*, 245–268. https://doi.org/10.1029/144GM16

Von Damm, K. L., Oosting, S. E., Kozlowski, R., Buttermore, L. G., Colodner, D. C., Edmonds, H. N., et al. (1995). Evolution of East Pacific Rise hydrothermal vent fluids following a volcanic eruption. *Nature*, *375*(6526), 47–50. https://doi.org/10.1038/375047a0

Wang, S., Chang, L., Wu, T., & Tao, C. (2020). Progressive dissolution of titanomagnetite in high-temperature hydrothermal vents dramatically reduces magnetization of basaltic ocean crust. *Geophysical Research Letters*, *47*(8), 1–11. https://doi.org/10.1029/2020GL087578

Wessel, P., Luis, J. F., Uieda, L., Scharroo, R., Wobbe, F., Smith, W. H. F., & Tian, D. (2019). The Generic Mapping Tools version 6. *Geochemistry, Geophysics, Geosystems*, *20*(11), 5556–5564. https://doi.org/10.1029/2019GC008515

White, S. M., Haymon, R. M., & Carbotte, S. (2006). A new view of ridge segmentation and near-axis volcanism at the East Pacific Rise, 8°–12°N, from EM300 multibeam bathymetry. *Geochemistry, Geophysics, Geosystems*, *7*(12), Q12O05. https://doi.org/10.1029/2006GC001407

Williams, C. M., Tivey, M. A., Schouten, H., & Fornari, D. J. (2008). Central anomaly magnetization high documentation of crustal accretion along the east Pacific rise (9°55′–9°25′N). *Geochemistry, Geophysics, Geosystems*, *9*(4), Q04015. https://doi.org/10.1029/2007GC001611

Wu, J., Parnell-Turner, R. E., Fornari, D. J., Kurras, G., Berrios-Rivera, N., Barreyre, T., & McDermott, J. M. (2022). Extent and volume of lava flows erupted at 9°50′N, east Pacific Rise in 2005–2006 from autonomous underwater vehicle surveys. *Geochemistry, Geophysics, Geosystems*, *23*(3), 1–35. https://doi.org/10.1029/2021gc010213

Xu, M., Canales, J., Carbotte, S. M., Carton, H., Nedimović, M. R., & Mutter, J. C. (2014). Variations in axial magma lens properties along the East Pacific Rise (9°30′N–10°00′N) from swath 3-D seismic imaging and 1-D waveform inversion. *Journal of Geophysical Research: Solid Earth*, *119*(4), 2721–2744. https://doi.org/10.1002/2013JB010730

Ziegler, L. B., Constable, C. G., Johnson, C. L., & Tauxe, L. (2011). PADM2M: A penalized maximum likelihood model of the 0–2 Ma palaeomagnetic axial dipole moment. *Geophysical Journal International*, *184*(3), 1069–1089. https://doi.org/10.1111/j.1365-246X.2010.04905.x